



Article

A Trace Element Classification Tree for Chalcopyrite from Oktyabrsk Deposit, Norilsk–Talnakh Ore District, Russia: LA-ICPMS Study

Alexander E. Marfin ^{1,2,*}, Alexei V. Ivanov ¹ , Vera D. Abramova ³, Tatiana N. Anziferova ^{1,3}, Tatiana A. Radomskaya ⁴, Tamara Y. Yakich ⁵  and Ksenia V. Bestemianova ⁶

¹ Institute of the Earth's Crust, Siberian Branch of the Russian Academy of Sciences, 664033 Irkutsk, Russia; aivanov@crust.irk.ru (A.V.I.); antsifer@yandex.ru (T.N.A.)

² Institute of Experimental Mineralogy, Russian Academy of Sciences, 142432 Chernogolovka, Russia

³ Institute of Geology of Ore Deposits Mineralogy, Petrography, and Geochemistry, Russian Academy of Sciences, 119017 Moscow, Russia; winterrain@rambler.ru

⁴ A.P. Vinogradov Institute of Geochemistry, Siberian Branch of the Russian Academy of Sciences, 664033 Irkutsk, Russia; taniaojigova@mail.ru

⁵ School of Earth Sciences & Engineering, Division for Geology, Tomsk Polytechnic University, 634050 Tomsk, Russia; cherkasovatu@tpu.ru

⁶ Faculty of Geology and Geography, National Research Tomsk State University, 634050 Tomsk, Russia; ksenijavt@mail.ru

* Correspondence: marfin1309@gmail.com

Received: 13 July 2020; Accepted: 11 August 2020; Published: 14 August 2020



Abstract: The Oktyabrsk PGE-Cu-Ni deposit is one of the largest resources in the Norilsk–Talnakh ore district, Russia, and it is viewed as an ore giant on a global scale. It contains three types of ores: massive, disseminated and veinlet-disseminated. The two former ore types were formed by a liquation process, whereas the latter was associated with fluid-induced selective metasomatic replacement of metamorphosed wall rocks. One of the major ore minerals in all ore types is chalcopyrite. In this study, we determined concentrations of trace elements in this mineral using laser ablation inductively coupled plasma mass spectrometry. It appeared that standard geochemical tools, such as plotting the data in the form of diagrams of normalized concentrations, binary and ternary plots, do not allow one to distinguish chalcopyrite from visually and genetically different ore types. In contrast, more advanced statistical methods such as cluster analysis show different groupings of elements for each ore type. Based on the element clustering, a classification tree was suggested, which allowed for the differentiation of massive, disseminated and veinlet-disseminated ore types of the Oktyabrsk deposit by Se, Te, Cd and Pb concentrations in chalcopyrite with a success rate of 86%. The general feature is that chalcopyrite of veinlet-disseminated ore is poorer in these elements compared to chalcopyrite of the two other ore types. Chalcopyrite of massive ore is poorer in Se and Te when compared to chalcopyrite of disseminated ore.

Keywords: Talnakh; Siberian flood basalts; LA-ICPMS; sulfide; chalcopyrite; cluster analysis; classification tree

1. Introduction

Chalcopyrite is the main ore mineral of copper, which is found in a wide number of deposits of various genesis on a global scale [1]. However, unlike pyrite [2–11], elemental data for chalcopyrite are limited [1,12–19]. The proposed genetic classifications in these studies were based on a limited number of elements, such as Zn, Cd and Se. In this study, we use laser ablation inductively coupled

plasma mass spectrometry (LA-ICPMS) to determine a wide range of trace elements (Ti, Mn, Co, Ni, Zn, Se, Mo, Ag, Cd, Sn, Te, Tl, Bi, Pb) in chalcopyrite from three major types of ore distinguished at the Oktyabrsk deposit in the Norilsk–Talnakh ore district, Russia, namely: massive, disseminated and veinlet-disseminated. The two former ore types are considered to be formed by sulfide–silicate immiscibility (liquation) [20–22], whereas the latter type is likely of contact metamorphic–metasomatic origin [23]. Using standard statistical approaches (calculation of the mean, median, the spread of the data, binary plots) and previously proposed classification schemes based on binary and ternary plots do not allow for the differentiation of the ore types by trace element abundances in chalcopyrite. Therefore, we use an advanced method based on cluster analysis and a classification tree approach, which allowed us to distinguish different ore types with a high success rate. Similar approaches were shown to be successful for the classification of garnets [24,25] and pyrite [11]. When large databases are available, such as in case of garnets [24,25], a meta-analysis may be applied [26]. Our study contributes to the topic of statistical analysis of complex data and provides new information on one of the largest global-scale Cu-Ni-PGE deposits.

2. Geological Background

2.1. Geology of the Oktyabrsk Deposit

The Oktyabrsk copper–nickel deposit with Pt-Pd mineralization is confined to the Kharaelakh intrusion (Figure 1). Its age of 251.71 ± 0.31 Ma (2σ external error including ^{238}U decay constant) was determined using chemical abrasion isotope dilution thermal ionization mass-spectrometry (CA-ID-TIMS) on zircon [27]. According to paleomagnetic data, the Kharaelakh intrusion is slightly older than other ore-bearing intrusions in the Norilsk–Talnakh ore district [28], though the difference in age is too small to be resolved by U-Pb data [27]. The rocks of the Kharaelakh intrusion occur within Devonian sediments, which are represented by terrigenous, carbonate and evaporite sediments. The intrusion falls at a gentle angle to the east, in the direction of the Norilsk–Kharaelakh fault. The average thickness of the Kharaelakh intrusion is 150 m. The intrusion has a pronounced layered structure. The rocks are represented by the following petrographic varieties: contact, taxite, picrite (also named plagiodunite and plagiowehrlite) and gabbrodolerite [20,21,29–33]. A detailed analysis of the geology, petrography, geochemistry, and isotopic characteristics of the intrusion and ores is beyond the scope of this paper and can be found elsewhere [34–47].

2.2. Three Types of Sulfide Ores

The following ore types are distinguished at the Oktyabrsk deposit [46]: massive, disseminated and veinlet-disseminated (from bottom to top, Figure 1). The massive (rich) copper–nickel ores are found at the lower part of the intrusion, and often are localized within the metasomatic and metamorphic rocks of the lower endo- and exo-contact or even within the Devonian sedimentary rocks of the Mantur and Kureika formations. Massive ore is composed of 70–90% sulfides (pyrrhotite, chalcopyrite, pentlandite, less often galena, talnakhite, heazlewoodite, bornite, chalcocite). The thickness of the horizon of the massive ores varies from the first tens of centimeters to 54 m. The massive ores are also found in some other parts of the intrusion, where they are represented by small veinlet bodies up to a few meters thick. It is assumed that sulfide melts were squeezed out along tectonic cracks. The following subtypes of the massive ores are distinguished by the ratio of ore minerals: (1) pyrrhotite (Figure 2a,b), (2) chalcopyrite (Figure 2c), (3) galena–chalcopyrite (talnakhite, bornite), and (4) pentlandite–(heazlewoodite)–bornite–chalcocite. In subordinate quantities, calcite, gypsum, minerals of the chlorite group, magnetite, titanomagnetite, and ilmenite are present as inclusions in the massive ores [45].

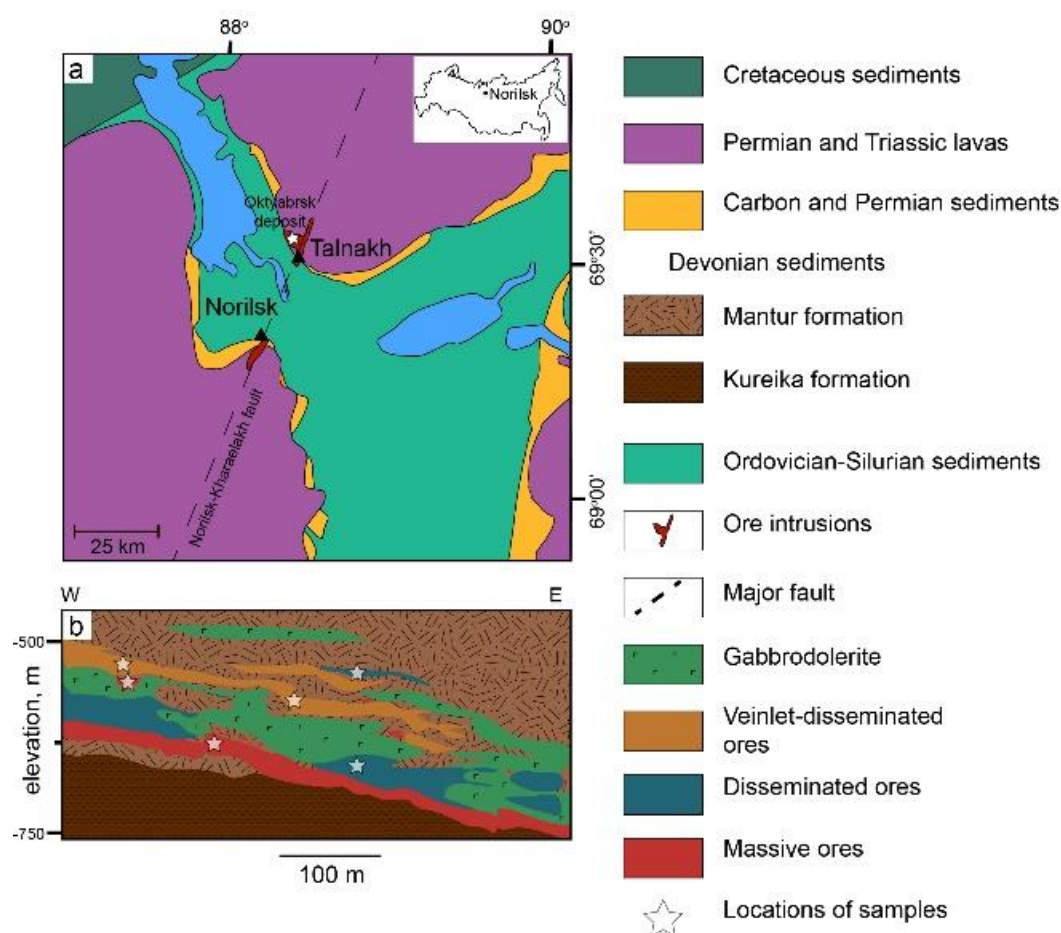


Figure 1. A schematic geologic map of the studied region (a) and a geologic cross-section of the Oktyabrsk deposit hosted by the Kharaelakh intrusion and its metamorphic aureole (b) based on [48]. Gabbrodolerites of the Kharaelakh intrusion were dated by CA-ID-TIMS on zircon to 251.71 ± 0.31 Ma (2σ external error including ^{238}U decay constant) [27]. Coeval, though with much large uncertainty, dates were obtained by U-Pb LA-ICPMS on metamorphic minerals of the veinlet-disseminated ores [49].

The disseminated type of ore is localized sometimes in contact gabbrodolerites and olivine-free gabbrodolerites (Figure 2d,e), but more often in picrites and taxitic gabbrodolerites (Figure 2f). Sulfides with a size of 0.1–2 mm are found in interstitial of silicates and as separate blobs up to 40–50 mm. Disseminated ores also occur in taxites where sulfide blobs are generally larger in size.

Veinlet-disseminated ores are found in the frontal part of the intrusion and above the intrusion within the contact metamorphic and metasomatic aureole of the Kharaelakh intrusion. Ores, which contain up to 30–50% of sulfides by volume, are located within hornfels and metasomatically altered Devonian sediments. By sulfide minerals, the veinlet-disseminated ores are (1) pyrrhotite, (2) chalcopyrite–pyrrhotite, (3) pyrrhotite–chalcopyrite (Figure 2g–j), (4) pentlandite–chalcopyrite, (5) millerite–pyrite–chalcopyrite, (6) millerite–bornite–chalcopyrite and (7) cubanite–chalcopyrite subtypes.

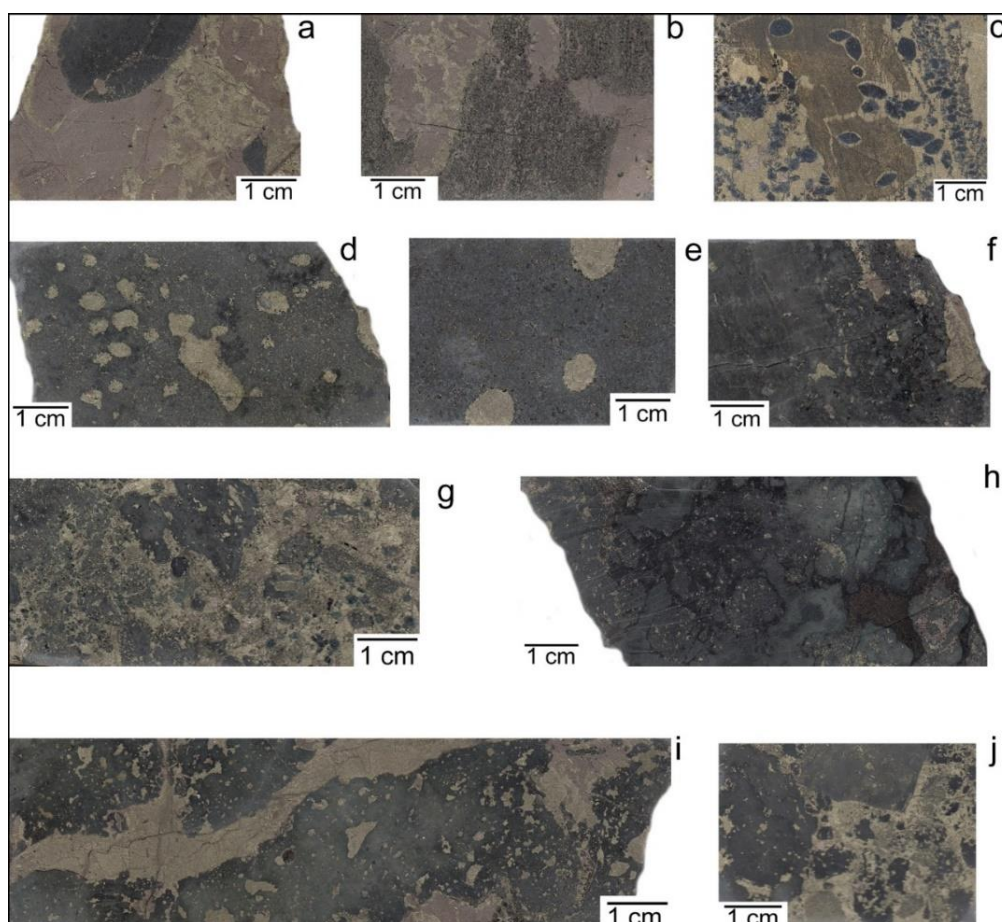


Figure 2. Studied ore types of the Oktyabrsk deposit. (a–c)—massive ores ((a,b)—pyrrhotite dominated, (c)—chalcopyrite dominated); (d–f)—disseminated ores ((d)—in contact gabbrodolerites, (e)—in olivine-free gabbrodolerites, (f)—in picrites); (g–j)—veinlet-disseminated ores (pyrrhotite–chalcopyrite subtype) in carbonate skarns. In (a–c): pyrrhotite in groundmass with the emulsion phase of chalcopyrite is indicative of coeval precipitation (massive texture) at the bottom part of the intrusion. In (d–e): pyrrhotite–pentlandite–chalcopyrite drops are typical for the upper contact of the intrusion. In (f): pyrrhotite–pentlandite–chalcopyrite drops of the intermediate part of the intrusion. In (g–j): skarn-like rocks.

3. Methods

3.1. SEM Analyses

Major element analyses and back scattered electron (BSE) images were taken using a Tescan Vega 3 SBU scanning electron microscope (SEM) equipped with an energy dispersive spectrometer (EDS) of Oxford Instruments (Abingdon, UK) with an Aztec-based system of microanalysis. The operating conditions were in the high-vacuum mode ($<9 \times 10^{-3}$ Pa) at an accelerating voltage of 20 kV with a high resolution and a distance of 15 mm.

SEM EDS analyses and BSE images were used for the two reasons: first, for selection and a visual control of minerals for the LA-ICPMS study and, second, for determination of iron content used as an internal standard in LA-ICPMS. An example of representative BSE images of chalcopyrite from different types of ores is shown in Figure 3.

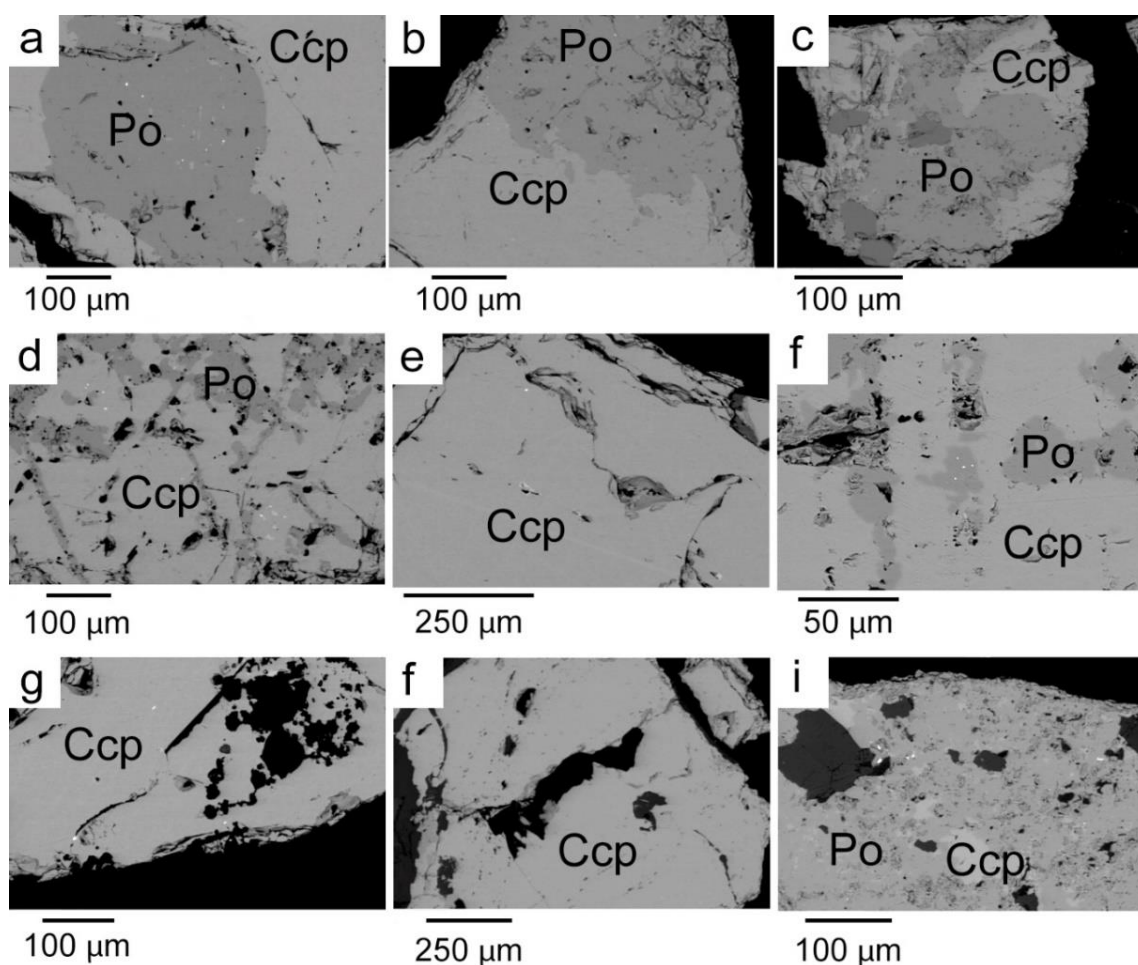


Figure 3. BSE images of chalcopyrite grains of massive (a–c), disseminated (d–f) and veinlet-disseminated (g–i) ores, respectively. Ccp—chalcopyrite, Po—pyrrhotite. Pentlandite is also present as small-size flames, which are too small to be indicated at the selected scale.

3.2. LA-ICPMS Analysis

The concentrations of ^{29}Si , ^{55}Mn , ^{59}Co , ^{60}Ni , ^{65}Cu , ^{66}Zn , ^{77}Se , ^{95}Mo , ^{107}Ag , ^{111}Cd , ^{118}Sn , ^{125}Te , ^{205}Tl , ^{208}Pb , ^{209}Bi in sulfides were determined by LA-ICPMS at the Laboratory of Mineral Analysis of Institute of Geology of Ore Deposits Mineralogy, Petrography, and Geochemistry, Russian Academy of Sciences. The LA-ICPMS system consists of a quadrupole mass spectrometer Thermo Xseries2 equipped with a New Wave 213 laser instrument. Selected isotopes do not contain a significant isobaric and molecular interference.

For external calibration, the standard reference materials (SRM) UQAC FeS-1 (University of Quebec in Chicoutimi, Canada), GSD-1G and STD GL-3, produced from natural sulfide powder and doped with trace elements, were used. MASS-1 polymetal sulfide (USGS) was used for verification of the results.

LA-ICPMS analyses were conducted using an 80 μm beam diameter for spots and 40–65 μm for lines, a laser frequency of 15 Hz, 5–7 J/cm^2 energy density and a 7 $\mu\text{m}/\text{s}$ ablation speed for lines. The carrier gas consists of a mixture of helium (0.7 L/min) and argon (0.85 L/min). Acquisition time in a spot mode was 30 s for the backgrounds, 60 s for the mineral analysis and 30 s of washout. Each line profile preceded 30 s of background. The material was then analyzed using the ICPMS operating in a time-resolved mode using peak jumping and a dwell time of 10 ms/peak per element.

Signal quantification was carried out by Iolite software using iron content in each sulfide determined by the SEM-EDS as an internal standard. Minerals in the profiles through intergrowths

were calculated separately, avoiding areas of the contacts. In the case of detection of microinclusions in the LA-ICPMS spectra, the corresponding part of a spectrum was cut out off-line. The detection limits for LA-ICPMS analyses were calculated as three sigma times the background counts for the gas blank. Silicon was monitored to exclude silicate inclusions.

Figure 4 shows representative lines through sulfide minerals with the background of BSE images. It is seen that chalcopyrite (Ccp), pentlandite (Pn) and pyrrhotite (Po) are easily recognized by their corresponding element spectra. Furthermore, we focus on chalcopyrite data only, because this mineral occurs in all ore types in a significant amount.

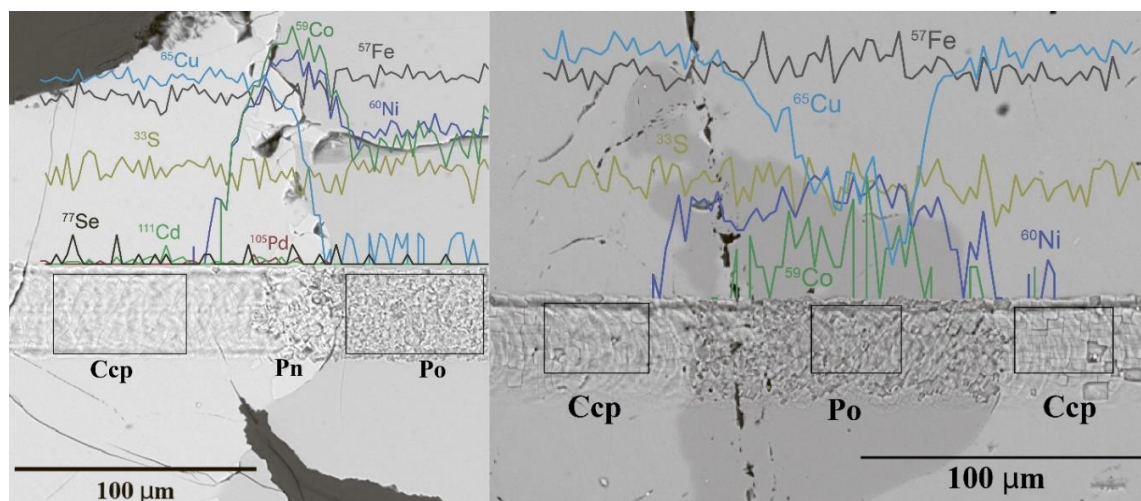


Figure 4. An example of two representative laser ablation lines on sulfide minerals. LA-ICPMS elemental spectra are shown by different colors. The LA-ICPMS data are superimposed on BSE images taken after the laser ablation analyses. Ccp—chalcopyrite, Po—pyrrhotite, Pn—pentlandite.

3.3. R Package

We used free RStudio software as a medium for R language. The used libraries were: “ggplot2” for making the violin plots, “cluster” for cluster analysis, “pvclust” for construction of classification trees, and “psych” for constructing correlation tables and binary plots <https://cran.r-project.org> (R for Windows v.R-4.0.2).

4. Results

Concentrations of 14 trace elements were determined in chalcopyrite of veinlet-disseminated (46 analyses), disseminated (25 analyses) and massive (16 analyses) ores (Table S1). Chalcopyrite of massive ores (32 analyses) was previously analyzed by LA-ICPMS for trace elements by [16]. Our new data are in good agreement with previously published results. However, for further internal consistency, we used only our new data. For each element of every ore type, violin plots were constructed (Figure 5, Figure S1).

Element concentrations of chalcopyrite of different ore types fully overlap. This is an unexpected result, because massive and disseminated ores are related to the process of silicate–sulfide immiscibility [20–22], whereas veinlet-disseminated ores are associated with the fluid-induced selective metasomatic replacement of metamorphosed wall rocks [23]. Thus, the source of metals of the two ore types is expected within the magma itself, whereas veinlet-disseminated ores should be affected by host rocks.

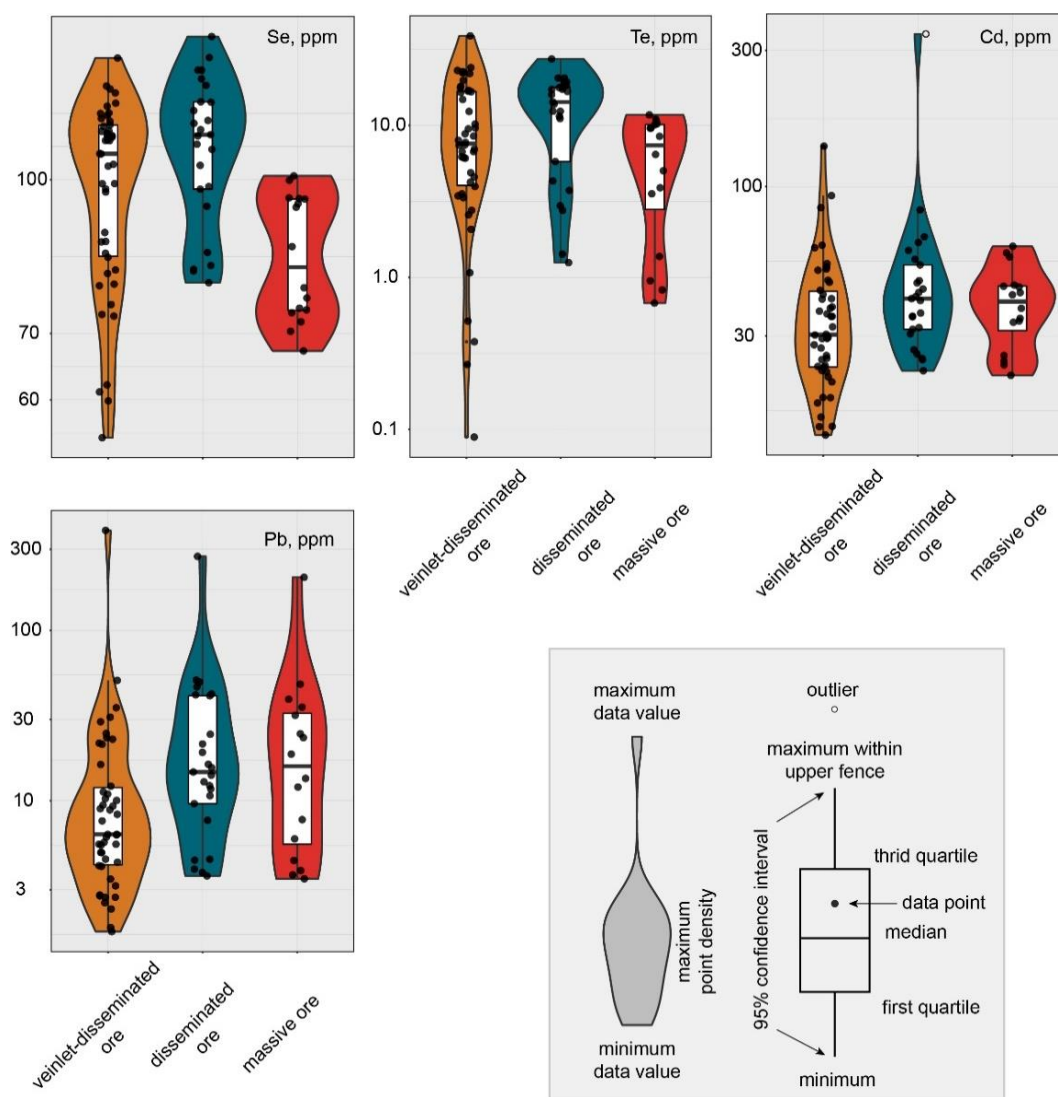


Figure 5. An example of violin plots for Se, Te, Cd, and Pb concentrations determined in chalcopyrite of the three ore types of the Oktyabrsk deposit. An explanation of the violin plot is in the low right-hand of the figure. Violin plots for other elements are shown in the Supplementary Figure S1. Colors are the same as in Figure 1b for the ore types.

Different elements may show coherent behavior depending on the process of crystallization of chalcopyrite. To test this, we applied cluster analysis, whose outcome is shown in Figure 6. Chalcopyrite of veinlet-disseminated, disseminated and massive ores is characterized by four, two and three clusters of elements with high similarity, respectively. Some element clustering can be easily explained by co-crystallization of particular mineral phases, though some spurious clustering could also occur (Table 1). For example, it is difficult to explain Ti-Sn, Ti-Mn-Mo and Mn-Ti-Zn-Ag clusters for chalcopyrite of veinlet-disseminated, disseminated and massive ores, respectively. Since, cluster analysis is merely a statistical tool, it inevitably produces some clusters that may have no geological meaning. Other clusters, such as Bi-Se-Te, Zn-Cd and Co-Ni in chalcopyrite of veinlet-disseminated ores, Ag-Co-Ni-Sn-Bi-Tl-Pb-Zn-Cd-Se-Te in chalcopyrite of disseminated ores and Co-Ni-Mo-Pb in chalcopyrite of massive ores, are explained by the presence of mineral phases observed in these ore types, which co-crystallized with chalcopyrite (Table 1). Se and Te form clusters in all three ore types because these two elements have similar geochemical behavior.

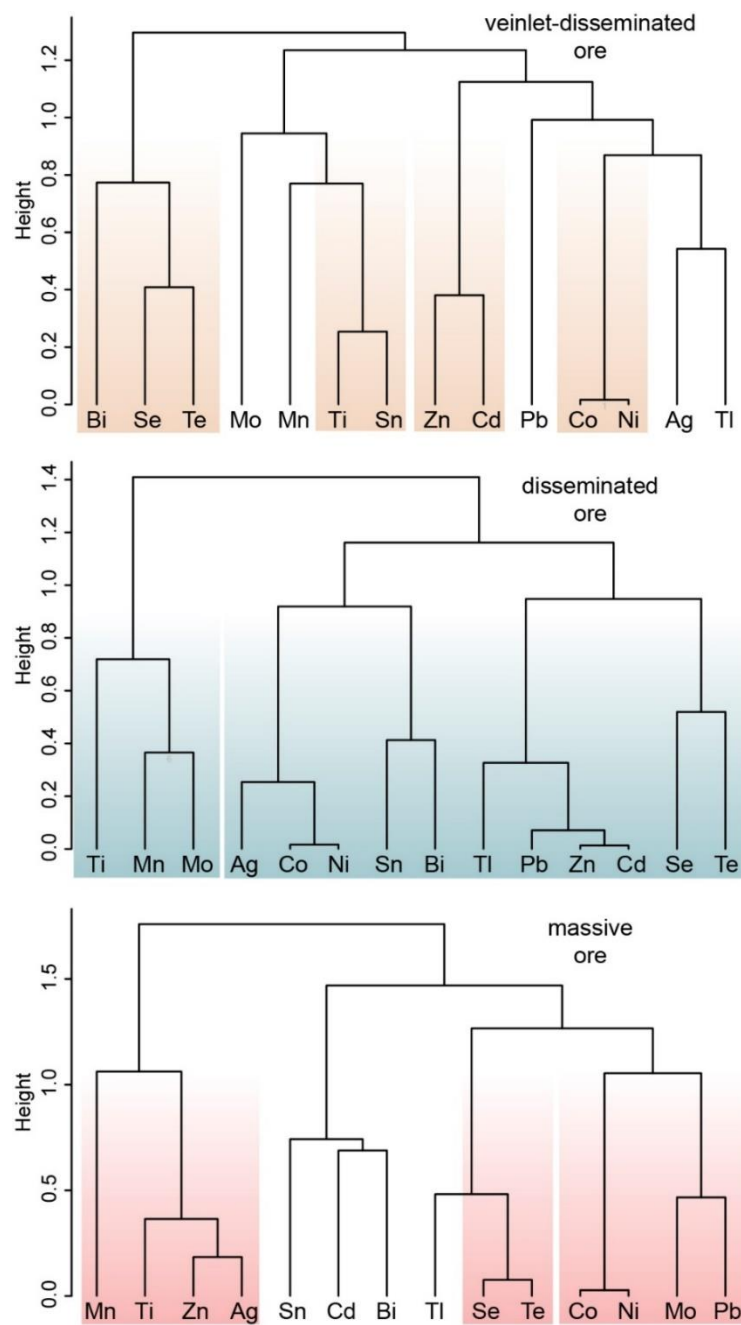


Figure 6. Cluster analysis of trace elements in chalcopyrite of veinlet-disseminated, disseminated and massive ores of the Oktyabrsk deposit. Colors underline elements with high similarity determined by cluster analysis.

For constructing a classification tree based on element clustering, we picked up several elements manually, which are the most common elements in all ore types. It appeared that using a limited number of elements, namely, Se, Te, Cd and Pb, allows satisfactory discrimination of the ore types with a success rate of 86%. The suggested classification tree is shown in Figure 7.

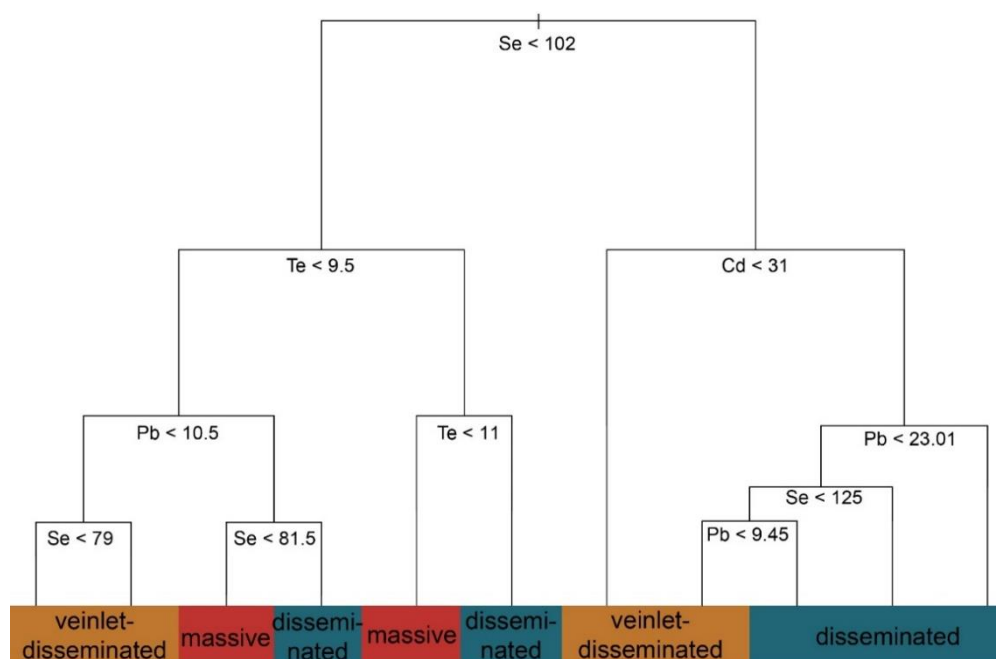


Figure 7. Suggested classification tree. Colors are chosen arbitrary to match the colors of ore types in Figure 1b.

Table 1. Results and interpretation of element clustering.

Type of Ores	Groups of Elements	Interpretation
Veinlet-disseminated ore	Bi-Se-Te	Co-crystallization of Bi-Te phases with chalcopyrite, isomorphism of Se and Te
	Ti-Sn	Spurious clustering?
	Zn-Cd	Co-crystallization of sphalerite with chalcopyrite, isomorphism of Cd and Zn
	Co-Ni	Co-crystallization of pentlandite and Co-pentlandite with chalcopyrite
Disseminated ore	Ti-Mn-Mo	Spurious clustering?
	Ag-Co-Ni-Sn-Bi-Tl-Pb-Zn-Cd-Se-Te	Initial crystallization of chalcopyrite from intermediate solid solution (ISS)
Massive ore	Mn-Ti-Zn-Ag	Rutile, ilmenite and Ti-magnetite
	Se-Te	Isomorphism of Se and Te in chalcopyrite
	Co-Ni-Mo-Pb	Co-crystallization of pentlandite, galena, isomorphism of Pb, Mo and Co

5. Discussion

A standard approach for the interpretation of multielement data includes (a) plotting of element concentrations normalized to a reference composition (chondrite, primitive mantle, mid-oceanic ridge basalt (MORB), etc.) (e.g., [1,50]) and (b) using binary and ternary plots (e.g., [51]). Such diagrams are used to visualize differences and similarities between different datasets and to draw genetic conclusions. However, in the case of our study, none of these diagrams show differences between chalcopyrite of the three different ore types of the Oktyabrsk deposit. As an example, we show a MORB sulfide-normalized diagram (Figure 8) and a set of binary plots with calculated Pearson correlation coefficients (Figure 9). It was already obvious from the violin plots (Figure 5, Figure S1) that such standard plots may not work.

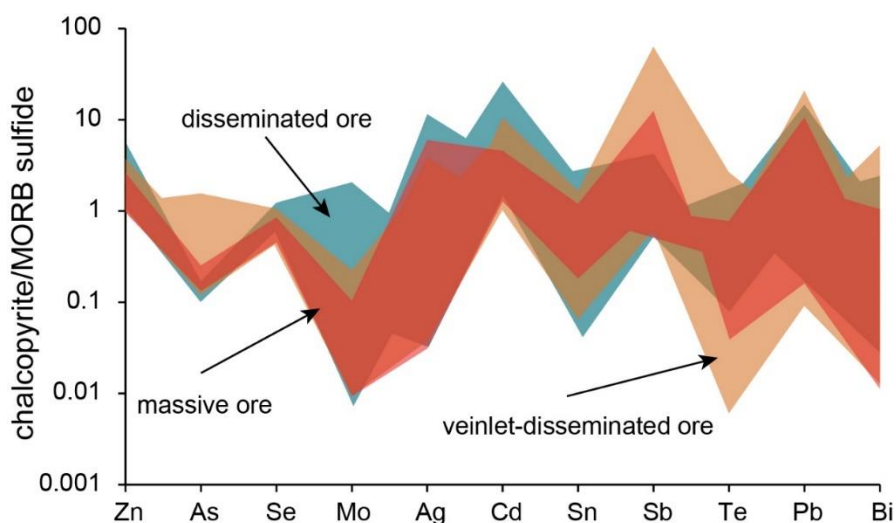


Figure 8. Mid ocean ridge basalt (MORB) sulfide-normalized concentration diagram for chalcopyrite of the three different ore types of the Oktyabrsk deposit. Normalized values of MORB sulfide are the mean value according to [52].

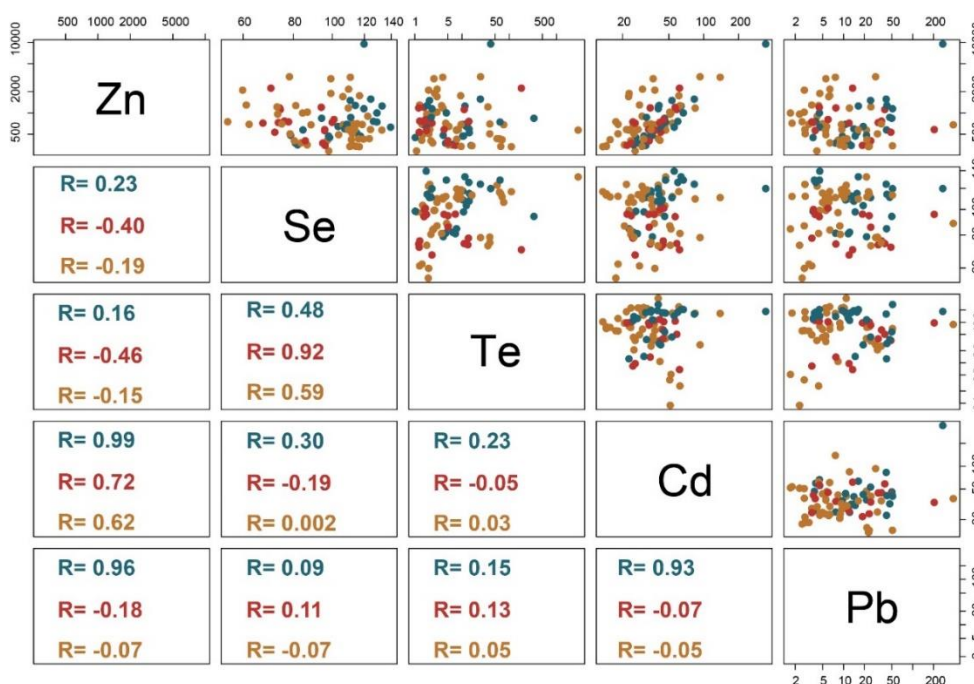


Figure 9. A fragment of Pearson correlation matrix and corresponding binary plots for chalcopyrite of the three different ore types of the Oktyabrsk deposit. The full correlation matrix is not provided due to its size. However, other elements show the same feature that the three different ore types cannot be distinguished from each other by using binary plots, though some elements show stronger correlations for chalcopyrite of disseminated ore (e.g., Zn-Cd, Zn-Pb) when compared to chalcopyrite of the other ore types. Colors in the caption (red, green, yellow) correspond to symbols of the same colors.

Previously, George et al. [1] suggested a genetic classification of chalcopyrite based on Zn and Cd concentrations (Figure 10). A stronger correlation coefficient for chalcopyrite of disseminated ore compared to the other two ore types gives hope to the idea that a Cd vs. Zn diagram could distinguish the disseminated ore type at least. However, all three ore types overlap on this diagram. Our data

spread over most of the fields with the majority of analyses located in the field of high crystallization temperature (Figure 10).

We also tried using the Se-Ni-Cd ternary genetic classification diagram of Duran et al. [13], suggested for discrimination between magmatic and hydrothermal chalcopyrite (Figure 11). In this diagram, half of analyses of chalcopyrite from the Oktyabrsk deposit are classified as magmatic and the other half as hydrothermal, irrespective of the ore type. Similarly, half of the analyses of chalcopyrite from massive ore of the Oktyabrsk deposit [16] fall into the hydrothermal type, whereas they should be within the magmatic field (Figure 11).

Using our classification tree (Figure 7), 90% of analyses of chalcopyrite from the Mansur et al. [16] database are correctly classified as belonging to the massive type of ore. This shows that the classification suggested in this study works, at least for the Oktyabrsk deposit, and is not dependent on the analytical set-up used for the analysis of trace element concentrations in chalcopyrite. However, our classification tree for the dataset of chalcopyrite analyses from Duran et al. [13] does not work. This shows that classifications such as those previously proposed by Duran et al. [13] or suggested in this study are dependent on the type of particular deposits. Our classification tree will likely work for the so-called Norilsk type of deposits, but may not be applicable for other types of deposits. The problem of using chalcopyrite for genetic classification is in the limited amount of empirical data. Our study also shows that interpretation of complex trace element data in chalcopyrite should be conducted using advanced statistical methods.

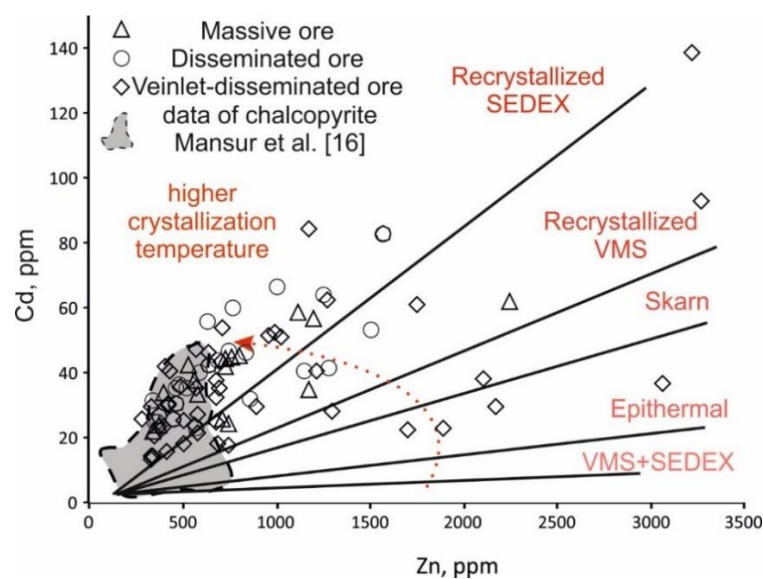


Figure 10. Binary classification diagram based on Cd and Zn concentrations in chalcopyrite from the Oktyabrsk deposit, suggested by the authors of [1].

Based on the suggested classification tree and known mineral associations in the different ore types, some ideas regarding the behavior of elements can be suggested. For example, chalcopyrite of disseminated ore is richer on average in Cd and Pb than chalcopyrite of the other two ore types. This is probably because the initial sulfide melt was rich in these elements and chalcopyrite crystallized before galena. Accumulation of sulfide drops to form massive ore, whose chalcopyrite is poorer on average in Cd and Pb when compared to chalcopyrite of disseminated ore, occurred after the beginning of galena crystallization. It was shown experimentally that cooling of sulfide melt from 700 °C to 400 °C leads to increase in Cu/Pb ratio in melt by a factor of 3, suggesting galena crystallization at higher temperatures than chalcopyrite [53]. As for the distribution of Se and Te in chalcopyrite, it is considered that Se is homogeneously distributed between monosulfide solid solution (MSS) and intermediate solid solution (ISS), whereas Te is favorably distributed to ISS [52]. Due to this, there is no difference

between chalcopyrite of disseminated and massive ores in terms of these elements because these ores are the product of the evolution of MSS. Chalcopyrite of veinlet-disseminated ores is poorer on average in Te than chalcopyrite of the other two types. This may show that veinlet-disseminated ore is not a product of the evolution of MSS and is related to another process, for example, metamorphism, as suggested by the authors of [49].

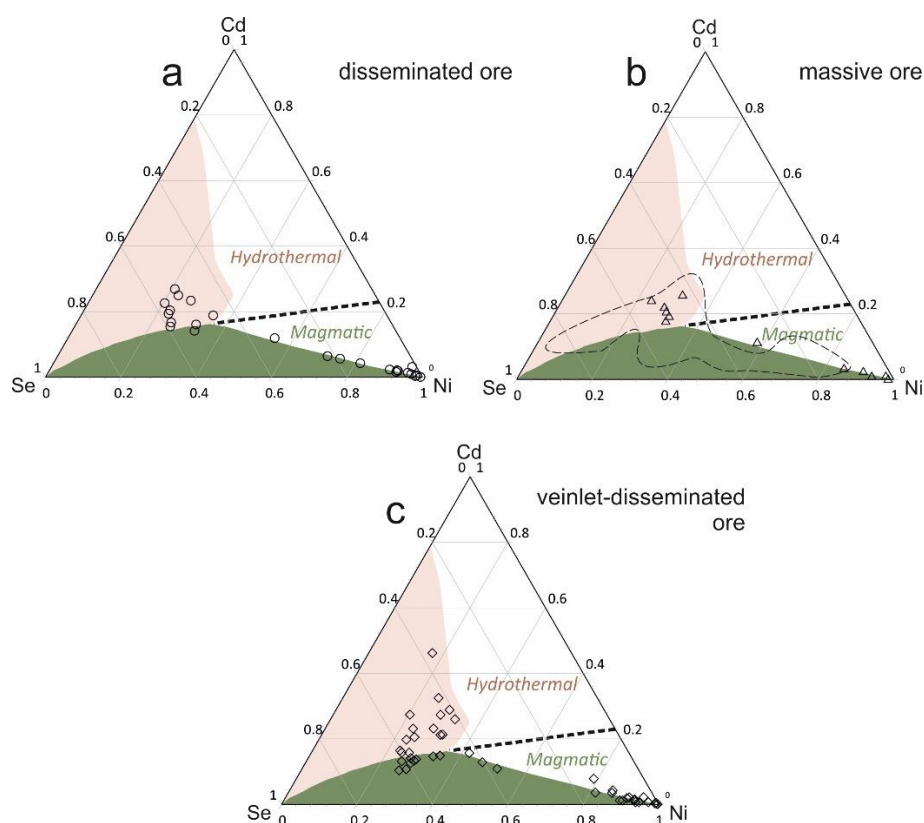


Figure 11. Ternary classification diagram based on concentrations of Cd, Se and Ni, according to the authors of [13]. The major idea of this classification is that the apexes trending to Ni and Cd are characteristics of magmatic and hydrothermal deposits, respectively. The apex trending towards Se was not given a genetic explanation by Duran et al. [13]. The thin dotted line is for the composition of chalcopyrite from massive ore of the Oktyabrsk deposit according to [16]. The bold dotted line discriminates hydrothermal and magmatic chalcopyrite according to [13]. Different symbols (circle, triangle and rhomb) are used for different ore types, respectively, disseminated, massive and veinlet-disseminated. (a) disseminated ore; (b) massive ore (c) veinlet-disseminated ore.

6. Conclusions

Trace element concentrations in chalcopyrite of massive, disseminated and veinlet-disseminated ores of the Oktyabrsk deposit of the Norilsk–Talnakh ore district are characterized by a large range of values. Conventional methods of representation of the trace element data such as plotting normalized concentrations or constructing binary and ternary diagrams do not allow for the separation of different ore types by trace element data in chalcopyrite. Thus, we suggested using more advanced statistics based on cluster analysis and a classification tree to distinguish chalcopyrite of different types of ores. Using the suggested classification tree allows separation of chalcopyrite from three types of ores with a success rate of 86%. A test on an independently published trace element dataset for chalcopyrite from massive ore of the same deposit shows a 90% of success rate for identifying the correct ore type. Overall, our study shows that (1) chalcopyrite is potentially useful for genetic classification and (2) advanced

statistical methods are superior to using simple diagrams, especially when complex analytical data are interpreted.

Supplementary Materials: The following are available online at <http://www.mdpi.com/2075-163X/10/8/716/s1>, Figure S1: Violin-plot of three types of ores, Oktyabrsk deposit, Table S1: Trace-elements compositions of chalcopyrite from three types ores, Oktyabrsk deposit.

Author Contributions: Conceptualization, A.E.M., A.V.I., V.D.A.; methodology, A.E.M., V.D.A., T.N.A., T.A.R., T.Y.Y., K.V.B.; writing—original draft preparation, review and editing, A.E.M., A.V.I., V.D.A., T.Y.Y.; funding acquisition, A.E.M., A.V.I. All authors have read and agreed to the published version of the manuscript.

Funding: A.E.M. and T.Y.Y. were funded by the grant No. 19-35-90013 from the Russian Foundation for Basic Research and the Tomsk Polytechnic University Competitiveness Enhancement Program for SEM investigation.

Acknowledgments: We thank two anonymous reviewers for constructive criticism and useful suggestions.

Conflicts of Interest: The authors declare no conflict of interest.

References

1. George, L.L.; Cook, N.J.; Crowe, B.B.; Ciobanu, C.L. Trace elements in hydrothermal chalcopyrite. *Mineral. Mag.* **2018**, *82*, 59–88. [[CrossRef](#)]
2. Roberts, F.I. Trace element chemistry of pyrite: A useful guide to the occurrence of sulfide base metal mineralization. *J. Geochem. Explor.* **1982**, *17*, 49–62. [[CrossRef](#)]
3. Ho, S.E.; McQueen, K.G.; McNaughton, N.J.; Groves, D.I. Lead isotope systematics and pyrite trace element geochemistry of two granitoid-associated mesothermal gold deposits in the southeastern Lachlan fold belt. *Econ. Geol.* **1995**, *90*, 1818–1830. [[CrossRef](#)]
4. Large, R.R.; Danyushevsky, L.; Hollit, C.; Maslennikov, V.; Meffre, S.; Gilbert, S.; Bull, S.; Scott, R.; Emsbo, P.; Thomas, H.; et al. Gold and trace element zonation in pyrite using a laser imaging technique: Implications for the timing of gold in orogenic and Carlin-style sediment-hosted deposits. *Econ. Geol.* **2009**, *104*, 635–668. [[CrossRef](#)]
5. Koglin, N.; Frimmel, H.E.; Minter, W.L.; Brätz, H. Trace-element characteristics of different pyrite types in Mesoarchean to Palaeoproterozoic placer deposits. *Miner. Depos.* **2010**, *45*, 259–280. [[CrossRef](#)]
6. Berner, Z.A.; Puchelt, H.; Noeltner, T.; Kramar, U. Pyrite geochemistry in the Toarcian Posidonia Shale of south-west Germany: Evidence for contrasting trace-element patterns of diagenetic and syngenetic pyrites. *Sedimentology* **2013**, *60*, 548–573. [[CrossRef](#)]
7. Zhang, J.; Deng, J.; Chen, H.-y.; Yang, L.-q.; Cooke, D.; Danyushevsky, L.; Gong, Q.-j. LA-ICP-MS trace element analysis of pyrite from the Chang'an gold deposit, Sanjiang region, China: Implication for ore-forming process. *Gondwana Res.* **2014**, *26*, 557–575. [[CrossRef](#)]
8. Gregory, D.D.; Large, R.R.; Halpin, J.A.; Baturina, E.L.; Lyons, T.W.; Wu, S.; Danyushevsky, L.; Sack, P.J.; Chappaz, A.; Maslennikov, V.V.; et al. Trace element content of sedimentary pyrite in black shales. *Econ. Geol.* **2015**, *110*, 1389–1410. [[CrossRef](#)]
9. Keith, M.; Häckel, F.; Haase, K.M.; Schwarz-Schampera, U.; Klemd, R. Trace element systematics of pyrite from submarine hydrothermal vents. *Ore Geol. Rev.* **2016**, *72*, 728–745. [[CrossRef](#)]
10. Batori, M.B.I.; Gilbert, S.; Large, R.R.; Zaw, K. Textures and trace element composition of pyrite from the Bukit Botol volcanic-hosted massive sulphide deposit, Peninsular Malaysia. *J. Asian Earth Sci.* **2018**, *158*, 173–185. [[CrossRef](#)]
11. Dmitrijeva, M.; Cook, N.J.; Ehrig, K.; Ciobanu, C.L.; Metcalfe, A.V.; Kamenetsky, M.; Kamenetsky, V.S.; Gilbert, S. Multivariate statistical analysis of trace elements in pyrite: Prediction, bias and artefacts in defining mineral signatures. *Minerals* **2020**, *10*, 61. [[CrossRef](#)]
12. Butler, I.; Nesbitt, R. Trace element distributions in the chalcopyrite wall of a black smoker chimney: Insights from laser ablation inductively coupled plasma mass spectrometry (LA-ICP-MS). *Earth Planet. Sci. Lett.* **1999**, *167*, 335–345. [[CrossRef](#)]
13. Duran, C.J.; Dubé-Loubert, H.; Pagé, P.; Barnes, S.-J.; Roy, M.; Savard, D.; Cave, B.J.; Arguin, J.-P.; Mansur, E.T. Applications of trace element chemistry of pyrite and chalcopyrite in glacial sediments to mineral exploration targeting: Example from the Churchill Province, northern Quebec, Canada. *J. Geochem. Explor.* **2019**, *196*, 105–130. [[CrossRef](#)]

14. Hawley, J.; Nichol, I. Trace elements in pyrite, pyrrhotite and chalcopyrite of different ores. *Econ. Geol.* **1961**, *56*, 467–487. [[CrossRef](#)]
15. Huston, D.L.; Sie, S.H.; Suter, G.F.; Cooke, D.R.; Both, R.A. Trace elements in sulfide minerals from eastern Australian volcanic-hosted massive sulfide deposits; Part I, Proton microprobe analyses of pyrite, chalcopyrite, and sphalerite, and Part II, Selenium levels in pyrite; comparison with delta 34 S values and implications for the source of sulfur in volcanogenic hydrothermal systems. *Econ. Geol.* **1995**, *90*, 1167–1196. [[CrossRef](#)]
16. Mansur, E.T.; Barnes, S.-J.; Duran, C.J.; Sluzhenikin, S.F. Distribution of chalcophile and platinum-group elements among pyrrhotite, pentlandite, chalcopyrite and cubanite from the Noril'sk-Talnakh ores: Implications for the formation of platinum-group minerals. *Miner. Depos.* **2020**, *55*, 1215–1232. [[CrossRef](#)]
17. Maslennikov, V.; Maslennikova, S.; Large, R.; Danyushevsky, L. Study of trace element zonation in vent chimneys from the Silurian Yaman-Kasy volcanic-hosted massive sulfide deposit (Southern Urals, Russia) using laser ablation-inductively coupled plasma mass spectrometry (LA-ICPMS). *Econ. Geol.* **2009**, *104*, 1111–1141. [[CrossRef](#)]
18. Yano, R.I. Trace Element Distribution in Chalcopyrite-Bearing Porphyry and Skarn Deposits. Master's Thesis, University of Nevada, Reno, NV, USA, 2012.
19. Yuan, B.; Yang, Y.; Yu, H.; Zhao, Y.; Ding, Q.; Yang, J.; Tang, X. Geochemistry of pyrite and chalcopyrite from an active black smoker in 49.6 E Southwest Indian Ridge. *Mar. Geophys. Res.* **2018**, *39*, 441–461. [[CrossRef](#)]
20. Spiridonov, E. Ore-magmatic systems of the Noril'sk ore field. *Russ. Geol. Geophys.* **2010**, *51*, 1059–1077. [[CrossRef](#)]
21. Ryabov, V.; Shevko, A.Y.; Gora, M. *Trap Magmatism and Ore Formation in the Siberian Noril'sk Region: Volume 1. Trap Petrology*; Springer Science & Business Media: Berlin, Germany, 2014; Volume 3.
22. Naldrett, A.J. A model for the Ni-Cu-PGE ores of the Noril'sk region and its application to other areas of flood basalt. *Econ. Geol.* **1992**, *87*, 1945–1962. [[CrossRef](#)]
23. Lightfoot, P.C.; Zotov, I.A. Geological relationships between the intrusions, country rocks and Ni-Cu-PGE sulfides of the Kharealakh Intrusion, Noril'sk region: Implications for the role of sulfide differentiation and metasomatism in their genesis. *Northwest. Geol.* **2014**, *47*, 1–34.
24. Griffin, W.; Fisher, N.; Friedman, J.; O'Reilly, S.Y.; Ryan, C. Cr-pyropes garnets in the lithospheric mantle 2. Compositional populations and their distribution in time and space. *Geochem. Geophys. Geosyst.* **2002**, *3*, 1–35. [[CrossRef](#)]
25. Griffin, W.; Fisher, N.; Friedman, J.; Ryan, C.; O'Reilly, S. Cr-pyropes garnets in the lithospheric mantle. I. Compositional systematics and relations to tectonic setting. *J. Petrol.* **1999**, *40*, 679–704. [[CrossRef](#)]
26. Chasse, M.; Griffin, W.L.; Alard, O.; O'Reilly, S.Y.; Calas, G. Insights into the mantle geochemistry of scandium from a meta-analysis of garnet data. *Lithos* **2018**, *310*, 409–421. [[CrossRef](#)]
27. Burgess, S.D.; Bowring, S.A. High-precision geochronology confirms voluminous magmatism before, during, and after Earth's most severe extinction. *Sci. Adv.* **2015**, *1*, e1500470. [[CrossRef](#)]
28. Latyshev, A.; Rad'ko, V.; Veselovskiy, R.; Fetisova, A.; Pavlov, V. Correlation of the Permian-Triassic ore-bearing intrusions of the Noril'sk region with the volcanic sequence of the Siberian Traps based on the paleomagnetic data. *Econ. Geol.* **2020**. [[CrossRef](#)]
29. Turovtsev, D.M. *Contact Metamorphism of Noril'sk Intrusions*; Nauchnyi Mir: Moscow, Russia, 2002.
30. Sluzhenikin, S.; Krivolutsкая, N.; Rad'ko, V.; Malitch, K.; Distler, V.; Fedorenko, V. *Ultramafic–Mafic Intrusions, Volcanic Rocks and PGE–Cu–Ni Sulfide Deposits of the Noril'sk Province, Polar Siberia. Field Trip Guidebook*; Institute of Geology of Ore Deposits, Petrography, Mineralogy and Geochemistry: Yekaterinburg, Russia, 2014.
31. Rad'ko, V. Model of dynamic differentiation of intrusive traps in the northwestern Siberian platform. *Geol. Geofiz.* **1991**, *11*, 19–27.
32. Malitch, K.N.; Latypov, R.M.; Badanina, I.Y.; Sluzhenikin, S.F. Insights into ore genesis of Ni-Cu-PGE sulfide deposits of the Noril'sk Province (Russia): Evidence from copper and sulfur isotopes. *Lithos* **2014**, *204*, 172–187. [[CrossRef](#)]
33. Malitch, K.; Belousova, E.; Griffin, W.; Badanina, I.Y. Hafnium-neodymium constraints on source heterogeneity of the economic ultramafic-mafic Noril'sk-1 intrusion (Russia). *Lithos* **2013**, *164*, 36–46. [[CrossRef](#)]
34. Vaulin, L.; Sukhanova, E. Oktyabr'skoe Cu-Ni deposit. In *Okhrana i Razvedka Nedr*; Izdatel'stvo Nedra: Moscow, Russia, 1970; pp. 48–52.
35. Dodin, D.A.; Batuev, B.N. Geology and petrology of the Talhakh differentiated intrusions and their metamorphic aureoles. In *Petrology and Ore Resource Potential of the Talnakh and Noril'sk Differentiated Intrusions*; Nedra: Leningrad, Russia, 1971; pp. 31–100. (In Russian)

36. Zolotukhin, V.; Ryabov, V.; Vasil'ev, Y.R.; Shatkov, V. *Petrology of the Talnakh Ore-Bearing Differentiated Trap Intrusion*; Nauka: Novosibirsk, Russia, 1975.
37. Wooden, J.L.; Czamanske, G.K.; Bouse, R.M.; Likhachev, A.P.; Kunilov, V.E.; Lyul'ko, V. Pb isotope data indicate a complex, mantle origin for the Noril'sk-Talnakh ores, Siberia. *Econ. Geol.* **1992**, *87*, 1153–1165. [[CrossRef](#)]
38. Lightfoot, P.; Hawkesworth, C.; Hergt, J.; Naldrett, A.; Gorbachev, N.; Fedorenko, V.; Doherty, W. Remobilisation of the continental lithosphere by a mantle plume: Major-, trace-element, and Sr-, Nd-, and Pb-isotope evidence from picritic and tholeiitic lavas of the Noril'sk District, Siberian Trap, Russia. *Contrib. Mineral. Petrol.* **1993**, *114*, 171–188. [[CrossRef](#)]
39. Torgashin, A.; Lightfoot, P.; Naldrett, A. Geology of the massive and copper ores of the western part of the Oktyabr'sky deposit. *Ont. Geol. Surv. Spec. Publ.* **1994**, *5*, 231–242.
40. Walker, R.J.; Morgan, J.W.; Beary, E.S.; Smoliar, M.I.; Czamanske, G.K.; Horan, M.F. Applications of the ^{190}Pt - ^{186}Os isotope system to geochemistry and cosmochemistry. *Geochim. Cosmochim. Acta* **1997**, *61*, 4799–4807. [[CrossRef](#)]
41. Li, C.; Ripley, E.M.; Naldrett, A.J.; Schmitt, A.K.; Moore, C.H. Magmatic anhydrite-sulfide assemblages in the plumbing system of the Siberian Traps. *Geology* **2009**, *37*, 259–262. [[CrossRef](#)]
42. Malitch, K.N.; Belousova, E.A.; Griffin, W.L.; Badanina, I.Y.; Pearson, N.J.; Presnyakov, S.L.; Tuganova, E.V. Magmatic evolution of the ultramafic-mafic Kharaelakh intrusion (Siberian Craton, Russia): Insights from trace-element, U-Pb and Hf-isotope data on zircon. *Contrib. Mineral. Petrol.* **2010**, *159*, 753–768. [[CrossRef](#)]
43. Malitch, K.N.; Latypov, R.M. Re-Os and S isotope constraints on timing and source heterogeneity of PGE-Cu-Ni sulfide ores: A case study at the Talnakh ore junction, Noril'sk Province, Russia. *Can. Mineral.* **2011**, *49*, 1653–1677. [[CrossRef](#)]
44. Krivolutskaya, N.; Sobolev, A.; Mikhailov, V.; Plechova, A.; Kostitsyn, Y.A.; Roschina, I.; Fekiacova, Z. Parental melt of the Nadezhdinsky Formation: Geochemistry, petrology and connection with Cu-Ni deposits (Noril'sk area, Russia). *Chem. Geol.* **2012**, *302*, 87–105. [[CrossRef](#)]
45. Sluzhenikin, S.F.; Mokhov, A.V. Gold and silver in PGE-Cu-Ni and PGE ores of the Noril'sk deposits, Russia. *Miner. Depos.* **2015**, *50*, 465–492. [[CrossRef](#)]
46. Krivolutskaya, N.; Tolstykh, N.; Kedrovskaya, T.; Naumov, K.; Kubrakova, I.; Tyutyunnik, O.; Gongalsky, B.; Kovalchuk, E.; Magazina, L.; Bychkova, Y.; et al. World-class PGE-Cu-Ni Talnakh deposit: New data on the structure and unique mineralization of the south-western branch. *Minerals* **2018**, *8*, 124. [[CrossRef](#)]
47. Krivolutskaya, N.A.; Gongalsky, B.I.; Kedrovskaya, T.B.; Kubrakova, I.V.; Tyutyunnik, O.A.; Chikatueva, V.Y.; Bychkova, Y.V.; Magazina, L.; Kovalchuk, E.N.; Yakushev, A.I.; et al. Geology of the western flanks of the Oktyabr'skoe deposit, Noril'sk district, Russia: Evidence of a closed magmatic system. *Miner. Depos.* **2019**, *54*, 611–630. [[CrossRef](#)]
48. Miroshnikov, L.K.; Ufatova, Z.G.; Kirpichenkov, K.A. Seismic shooting in geodynamic zoning of the rock and ore mass in conditions of deep ore mines operation. *Min. Ind. J.* **2018**, *1*, 46–47. [[CrossRef](#)]
49. Marfin, A.E.; Ivanov, A.V.; Kamenetsky, V.S.; Abersteiner, A.; Yakich, T.Y.; Dudkin, T.V. Contact Metamorphic and Metasomatic Processes at the Kharaelakh Intrusion, Oktyabrsk Deposit, Norilsk-Talnakh Ore District: Application of Laser Ablation-Inductively Coupled Plasma-Mass Spectrometry Dating of Perovskite, Apatite, Garnet, and Titanite. *Econ. Geol.* **2020**. [[CrossRef](#)]
50. McDonough, W.F.; Sun, S.-S. The composition of the Earth. *Chem. Geol.* **1995**, *120*, 223–253. [[CrossRef](#)]
51. Pearce, J.A.; Harris, N.B.; Tindle, A.G. Trace element discrimination diagrams for the tectonic interpretation of granitic rocks. *J. Petrol.* **1984**, *25*, 956–983. [[CrossRef](#)]
52. Patten, C.; Barnes, S.-J.; Mathez, E.A.; Jenner, F.E. Partition coefficients of chalcophile elements between sulfide and silicate melts and the early crystallization history of sulfide liquid: LA-ICP-MS analysis of MORB sulfide droplets. *Chem. Geol.* **2013**, *358*, 170–188. [[CrossRef](#)]
53. Mavrogenes, J.; Frost, R.; Sparks, H.A. Experimental evidence of sulfide melt evolution via immiscibility and fractional crystallization. *Can. Mineral.* **2013**, *51*, 841–850. [[CrossRef](#)]

